ACS Catalysis

Research Article

pubs.acs.org/acscatalysis

Critical Influence of Nanofaceting on the Preparation and Performance of Supported Gold Catalysts

Miguel Tinoco,[†] Susana Fernandez-Garcia,[†] Miguel Lopez-Haro,[†,‡] Ana B. Hungria,[†] Xiaowei Chen,[†] Ginesa Blanco,[†] Jose A. Perez-Omil,[†] Sebastian E. Collins,[§] Hanako Okuno,[‡] and Jose J. Calvino*[,†]

[†]Departamento de Ciencia de los Materiales e Ingeniería Metalúrgica y Química Inorgánica, Facultad de Ciencias, Universidad de Cadiz, Campus Río San Pedro, E-11510, Puerto Real, Cádiz, Spain

[‡]University Grenoble Alpes, INAC-SP2M, and CEA, INAC-SP2M, LEMMA, F-38000 Grenoble, France

[§]Instituto de Desarrollo Tecnológico para la Industria Química (CONICET, UNL), Güemes, 3450, S3000GLN, Santa Fe, Argentina

Supporting Information

ABSTRACT: A partial transformation of the {100} surfaces of ceria nanocubes into a set of nanometer-heighted, {111}-bounded, peaks was achieved by an oxidation treatment at 600 °C. This particular type of surface nanostructuration allows the preparation of CeO_2 nanoparticles in which {111} nanofacets contribute significantly to their surface crystallography. This transformation of the surface structure plays a key influence on the behavior of ceria as a support of gold catalysts. Thus, the appearance of well-developed {111}-nanofacets leads to a much higher efficiency in the usage of this noble metal in the synthesis of catalysts when prepared by the deposition−precipitation method. Moreover, gold catalysts supported on the surface-reconstructed oxide present an intrinsic (per gold surface atom) CO oxidation activity much higher than that of catalysts prepared on the nontreated oxide.

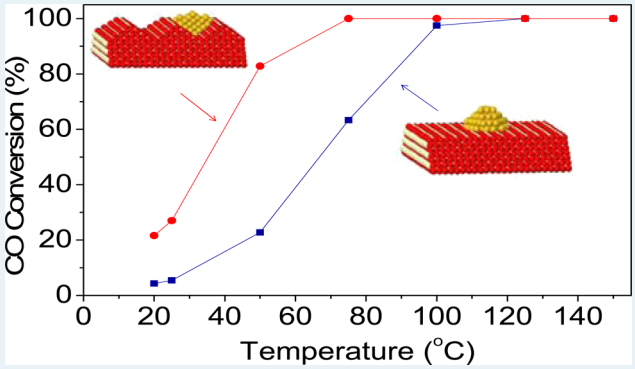

KEYWORDS: *ceria, gold, surfaces, catalysis, transmission electron microscopy*

INTRODUCTION

The exact crystallographic nature of the surfaces of oxide nanoparticles is currently considered to play a major influence on their chemical properties as well as on their performance as catalysts.[1−3] Particularly, the case of CeO_2 has been one of the most extensively studied, possibly due to the high technological impact of this reducible oxide in a variety of processes, e.g., in catalytic converters.[1−9] Thus, as a bare oxide, a number of studies have revealed changes in the reducibility of ceria, under hydrogen atmosphere, as a function of particle morphology.[10] In general, CeO_2 nanorods (NRs) have been reported to be more reducible than CeO_2 nanocubes (NCs) and these, in turn, to be more reducible than CeO_2 nano-octahedra (NOs).[1,3,10] Concerning catalytic performance, Aneggi et al.[11] have pointed out a parallel increase in the CO oxidation activity with the contribution of {100} type facets in a powder type CeO_2 sample. Likewise, differences in the activities for CO oxidation and water gas shift reactions have also been reported for Au catalysts supported on CeO_2−NRs, CeO_2−NCs, and CeO_2−NOs.[12−14]

Nevertheless, none of these studies have considered either the influence of the large differences in the particle dimensions between the different types of morphologies compared or the presence of contaminants at the surface, remnant from the synthesis process, which could largely influence the chemical properties of the shaped oxide nanoparticles. Thus, while CeO_2−NCs reported in those studies have been synthesized with sizes in the 10−30 nm range, CeO_2−NOs have usually ranged from 200 to 500 nm, i.e. an order of magnitude larger.[3,8,10,15,16] Therefore, while the CeO_2 {100} facets of NCs could be really considered as nanosized, this is not clearly the case of the {111} facets of NOs, which are much closer to that of conventional extended {111} facets. Moreover, Wu et al.[2] have reported the presence of an important phosphate signal in the Raman spectra of CeO_2−NOs, which could be attributed to residues of the Na_3PO_4 used during the preparation. Phosphorus is widely recognized as a very poisonous element in catalysis and acknowledged to be hard to remove from solids due to its extraordinary thermal stability.[17] Finally, it should be also mentioned that comparisons reported between Au catalysts supported on CeO_2 crystallites with different morphologies have not properly taken into account the differences between gold particle size distributions in the different catalysts.[13,14] Accordingly, comparisons between the functional properties of

Received: January 16, 2015
Revised: April 29, 2015
Published: April 30, 2015

© 2015 American Chemical Society

DOI: 10.1021/acscatal.5b00086
ACS Catal. 2015, 5, 3504−3513

CeO_2 or Au/CeO_2 catalysts derived from different morphologies deserve a more detailed consideration, by starting from materials that overcome the limitations just mentioned.

The surfaces of CeO_2−NCs are mostly dominated by {100} facets truncated at the edges and corners by {110} and {111} planes, respectively, which nevertheless represent only a very small contribution (below 10%) to the total exposed surface.[15] Both theoretical DFT calculations and experimental observations have revealed that {100}-CeO_2 surfaces are metastable and tend to reconstruct into {111}-related structures.[18−23] Moreover, according to Fronzi et al.[20] such transformation is enhanced under oxygen rich environments. On one hand, Crozier et al.[19] have observed that {110} CeO_2 surfaces can in fact be described in terms of a sawtooth like structure, comprising adjoined {111} nanofacets, which only flatten under reducing conditions to accommodate the corresponding oxygen vacancies. Therefore, it seems reasonable to expect that the reconstruction of {100} facets under appropriate oxidizing environments could be used as a route to prepare {111} nanofaceted CeO_2 starting from nanocubes.

In this contribution we report the results of this approach yet unexplored to the best of our knowledge, to prepare CeO_2 crystals with nanosized dimensions and neatly differing surface crystallography. Our results do not only confirm the adequacy of the new synthesis route but also illustrate the very high impact of surface nanostructuring on the performance of CeO_2 as a support of gold nanoparticles. In this respect, dramatic changes are confirmed related not only to the efficiency of CeO_2 to fix the supported gold phase, but also on the influence of surface crystallography on the final electronic state and catalytic performance of the deposited gold phase.

RESULTS AND DISCUSSION

Figure 1 shows transmission electron microscopy (TEM), a, and high angle annular dark field (HAADF), b−d, images representative of the starting CeO_2NC sample used in our study. This nano-oxide sample was prepared using a hydrothermal route, as described by Mai et al.[1] (details in the experimental section). Note how it is in fact constituted by cube shaped nanocrystals, Figure 1a. According to the spots observed in the digital diffraction pattern (DDP) of the HAADF-STEM image in Figure 1b, inset, the CeO_2 nanocrystals are imaged down the [001] zone axis. Hence, the flat facets of the cubes would correspond to {100} surfaces. Note also from this image the presence of truncations at the corners, which can be associated with {110} and {111} facets.[5,15,21] Since the {110} facets are imaged edge-on along this zone axis, the lateral extent of these {110} facets can be estimated to be of the order of 1.5 nm. HREM images recorded along the [110] zone axis, like that in Figure 1c and d, show the presence of both {100}, {111}, and {110} facets. The latter clearly presents, as previously mentioned,[19,21] a saw-tooth like structure made up of pretty short (<0.4 nm), subnanometer-sized, {111} planes. On its hand, the extent of {111} facets related to truncations at the corners of the cube is about 2.5 nm.

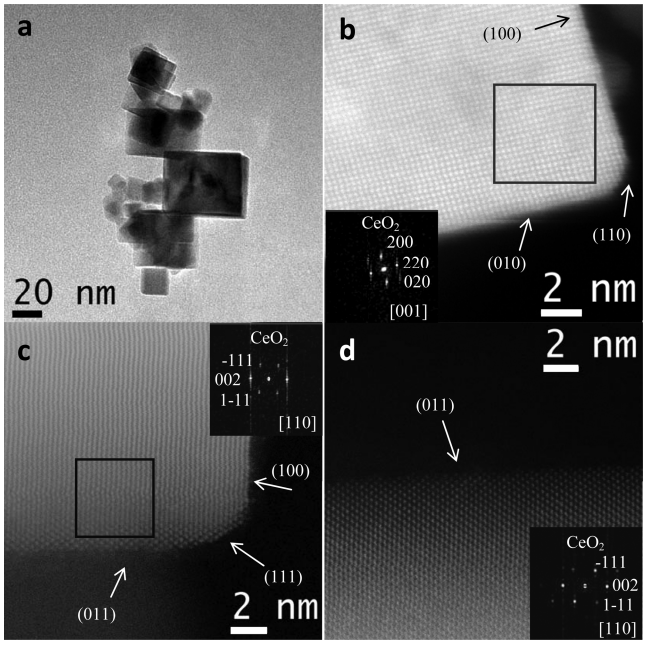

Figure 1. (S)TEM images of the CeO_2NC sample: (a) TEM image at low magnification, (b) HAADF-STEM image on the [001] zone axis, (c and d) HAADF-STEM images on the [110] zone axis.

The nanocrystal size distribution corresponding to this sample, as determined from the electron microscopy (HREM/HAADF-STEM) characterization studies, Figure S1(a) in the Supporting Information, spans over the 5−50 nm edge length range with an average value of L_{av} =19 ± 8 nm for this parameter. The volume-weighted average cube edge length estimated from the distribution amounts to 22 nm, a value in very good agreement with that determined from the XRD diagram of this sample, Figures S1(a) and S2. Moreover, from this distribution, a value of specific surface area of 33 $m^2 \cdot g^{-1}$ could be estimated assuming a cubic model for the oxide nanoparticles. This value is very close to the BET surface area determined experimentally from N_2 physisorption measurements, 38 $m^2 \cdot g^{-1}$, all of this indicating that the nanoparticle size distribution determined by STEM would satisfactorily represent the sample at a macroscopic level.

Apart from the nanocubes, it seems that some small and irregular nanoparticles are also present in the CeO_2NC sample (Figures 1a and S3). However, the analysis of electron tomography experiments, Figure S4, indicates that these are also cubic shaped oxide nanocrystals imaged along random crystallographic directions. Note how the small particle labeled as A in Figure S4(a) looks like rounded triangular in shape in the HAADF-STEM image, while, after the reconstruction of the tomographic tilt series, Figure S4(b), that nanocrystal clearly shows a corner-rounded cubic shape when it is correctly oriented and sliced. Therefore, tomography experiments demonstrate that nanoparticles that may not look cubic at first glance can in fact be cubic-shaped.

This starting CeO_2NC sample was treated for 1 h at 600 °C under flowing 5% O_2/He (60 $mL \cdot min^{-1}$) at atmospheric pressure. We will refer to this new sample as CeO_2NC600. As with the initial sample, a HREM/HAADF-STEM characterization study was performed on this oxide and the corresponding cube-length size distribution was established, which is displayed in Figure S1(b). Note that the average size of the cubes has increased up to 23 ± 13 nm. The volume averaged cube size determined from this distribution (33 nm) was quite close to the value determined from the corresponding XRD diagram, Figure S2. Likewise, the value of specific surface area which could be estimated from the distribution and a cube morphology model, 19 $m^2 \cdot g^{-1}$, is quite close to that determined experimentally, 18 $m^2 \cdot g^{-1}$. This also indicates that the whole set

DOI: 10.1021/acscatal.5b00086
ACS Catal. 2015, 5, 3504−3513

of recorded electron microscopy images reasonably represent the sample at the macroscopic level.

Aside from the oxide nanoparticle dimensions, HREM/HAADF-STEM images provided much more interesting information. Note first, HREM image in Figure 2a, that

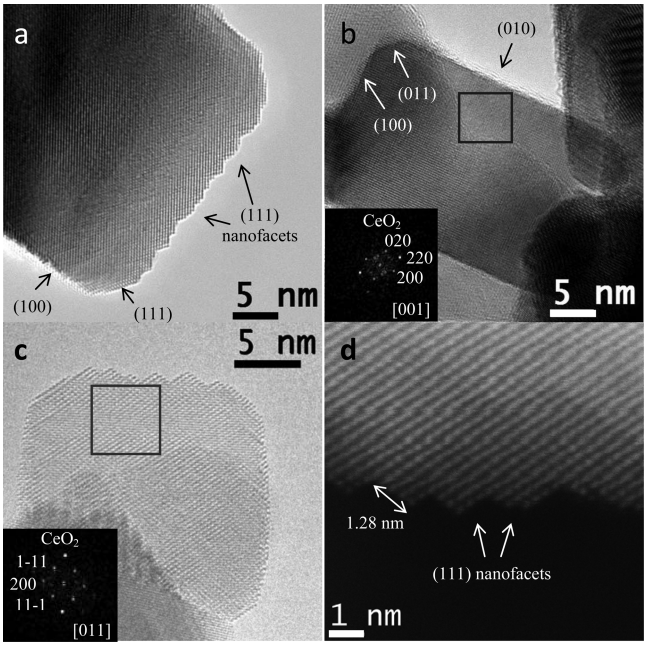

Figure 2. (S)TEM images of the CeO_2NC600 sample: (a) HREM image of the nanofacets, (b) HREM image on the [001] zone axis, (c) HREM image on the [011] zone axis, (d) HAADF-STEM image on the [011] zone axis.

although the nanocrystals of the treated CeO_2NC600 oxide retain a cube-like shape to a large extent (see also Figure S3 in the Supporting Information), surface roughness is now clearly appreciated on some surfaces. The more detailed structural view provided by these atomically revolved images, Figure 2a–d, indicates that this roughness is associated specifically to the {110} surfaces. Thus, in the HREM image along the [001] zone axis, Figure 2b, the two {100} facets appear still flat, as in the initial CeO_2NC oxide, before the oxidation treatment. In contrast, in the images recorded along the [110] zone axis, Figure 2c, the {100} surfaces appear flat but those corresponding to the {110} facets clearly show a zigzagged shape. In a detailed STEM study of as-prepared CeO_2 nanocubes, Bhatta et al.[24] reported the presence of saw-tooth like structures on the {110} edges. Nevertheless, they indicate that such structures were very rarely observed. In clear contrast, this zigzag structure affects most of the nanocubes in the oxidized CeO_2NC600 catalyst, being much more developed than in the initial CeO_2NC sample. The hills and valleys structure depicts now a larger depth, and the extent of the small {111} facets that limit this peculiar surface structure is, on average, also larger but still in the nanometer range (0.4–1 nm). The analysis of the HREM images along [001] indicates that the lateral extent of the {110} facets, onto which this complex system of {111} nanofacets develops, has increased up to roughly 3.5 nm, in average, corresponding to a value three times that in the initial, nontreated oxide. The extent of the {111} facets associated with truncations at the corners of the cube, which can be detected only in the HREM images along the [110] zone axis, has also increased from 2.5 nm in the CeO_2NC sample up to 4.5 nm in the CeO_2NC600 oxide.

Starting from a significant number of images of the bare catalysts, we have performed a statistical analysis of changes in geometrical parameters of the nanocubes (Figure 3). Note that

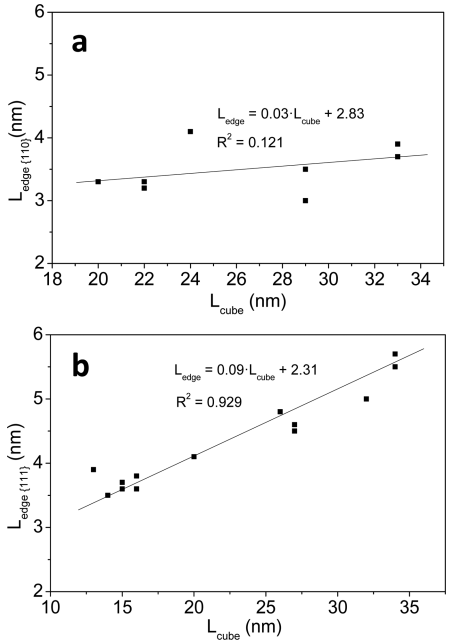

Figure 3. Lengths of the edges (L_{edge}) versus dimensions of the nanocubes (L_{cube}) measured from the (S)TEM images of the CeO_2NC600 sample recorded at different zone axes: (a) nanocube edges analyzed down the [100] zone axis, measuring the {110}-related truncations, (b) dimensions of the {111} facets related to corner rounding determined from (S)TEM images collected down [110] orientations.

the length of the {110} facets in the CeO_2NC600 catalyst shows only a weak dependence and very low correlation with nanocube edge length, Figure 3a, all the values falling in the range 3–5 nm and with an average of 3.5 nm. In contrast, there is a clear trend in the length of the {111} facets in the CeO_2NC600 catalyst with nanocube edge length, Figure 3b, with a correlation factor around 0.93. This length is about 3 nm in the smallest cubes (10–15 nm) but close to 6 nm in the cubes with sizes around 35 nm.

Concerning the height of the {111}-nanofacets, Figure 4, we have found no correlation of this parameter with the length of the cube edges. This height, which can be measured in terms of the number of {220} planes from the valleys to the summit, varies in the range 1–6 with an average about 3.5 (= 0.7 nm).

By combining this information with that coming from the cube edge length distribution established for each sample (Figure S1), we have made an estimate of the contribution of the different type of planes ({100}, {110}, and {111}) to the surface exposed by the nanocubes in the two catalysts, Table 1. Note that the contribution of the {100} facets decreases from 84% in CeO_2NC down to 75% in CeO_2NC600. The contribution of {110} facets increases by 8%, but it is not possible to make an estimate of its exact contribution to exposed surface area since in the CeO_2NC catalyst this is an atomically smooth surface but a complex system of {111} nanofacets in CeO_2NC600. Finally, the contribution of flat

DOI: 10.1021/acscatal.5b00086
ACS Catal. 2015, 5, 3504–3513

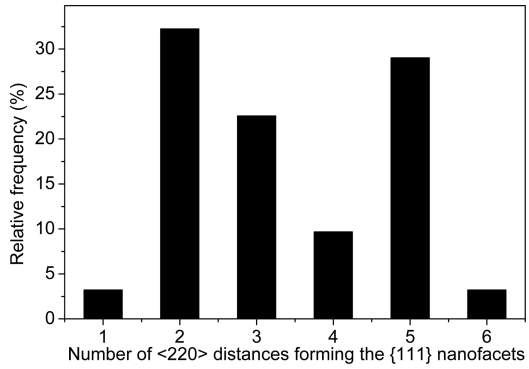

Figure 4. Statistical study of the variability of the heights of {111}-nanofacets.

Table 1. Contribution of the Different Exposed Planes to the Total Surface Area in the Different CeO_2 Nanocube Samples

facet	percentage (%) in CeO_2NC	percentage (%) in CeO_2NC600
{100}	84	75
{110}	16	24
{111}	<1	1

cube corner related {111} facets does not exceed 1% in CeO_2NC600.

It is clear from these results that the oxidizing treatment at 600 °C has induced a surface restructuration, which involves a significant increase in the contribution to the surface crystallography of {111} facets with nanometer dimensions that we could call nanofacets. These nanofacets comprise both those building-up on {110} facets associated with truncations of the cube edges, and the {111} facets corresponding to truncations at the cube corners.

In connection with the influence of shape on the catalytic activity in soot combustion of CeO_2 nanocrystals, Aneggi et al.[25] have recently reported the occurrence of corner rounding in CeO_2 nanocubes after aging in air at 750 °C. Such rounding was related to the presence of {110} type planes comprising high index planes. Our results indicate that this is in fact a progressive process, since {110} facets are already present in the nanocubes just as-prepared. Increasing oxidation temperature induces not only a growth of {110} type facets but also a change in their exact crystallographic nature. Thus, in the as-prepared nanocubes these are mostly atomically smooth {110} facets but after oxidation at 600 °C, as HREM images down the [110] zone axis direction clearly prove, they correspond to a complex system of {111} nanofacets. This is in fact a quite different crystallographic description for these surfaces, which are not definitely formed by high index planes or atomically stepped {111} extended surfaces. Isolated atomic steps could only be identified on the {111} planes present in the corners of the nanocubes. Our results also reveal that changes in the surface crystallography are already significant at much lower temperatures.

Due to the high relevance of surface modifications on the redox and catalytic behavior of CeO_2-related materials, TPR-H_2 and IR experiments were carried out to fully characterize such properties. The results of TPR-H_2 experiments performed on the CeO_2NC and CeO_2NC600 bare oxide samples (Figure S5) indicate that the former is slightly more reducible under hydrogen. Both TPRs show the same major peaks, but the temperatures corresponding to the reduction peaks observed in the CeO_2NC sample are all slightly shifted to lower temperatures. These results agree with previous observations by Aneggi et al.[25] Nevertheless, those variations might not only be related with the different surface crystallography of the two samples, but also with changes in particle size.

As observed in Figure S6, the two nanocube oxide samples, CeO_2NC and CeO_2NC600, show FTIR bands in the frequency range characteristic of carbonate species (1200−1600 cm^{-1}). Peaks attributable to polydentate/monodentate carbonates ($\nu_{as}(CO_3)$ = 1465 cm^{-1} and $\nu_{as}(CO_3)$ = 1394 cm^{-1}) and bidentate carbonates (about $\nu_{as}(CO_3)$ = 1550 cm^{-1} and $\nu_{as}(CO_3)$ = 1357 cm^{-1}) are observed.[26−31] Note that the intensity of these bands is very similar in both samples, which suggests a comparable carbonation degree. Differences in the relative intensities of the two types of carbonate species between the two samples can be related to their differences in the surface crystallography. Regarding hydroxyl groups, IR bands are also observed (3630 and 3658 cm^{-1}) with similar intensities in the two oxide nanocube samples.

Both nano-oxide samples, CeO_2NC and CeO_2NC600, were used to prepare a ceria-supported gold catalyst by the widely used deposition−precipitation (DP) method (details in the Methods). The Au loading targeted in these preparations was 1.5 wt %; however, both catalysts retained a lower amount of active metal on their surfaces. Thus, the catalyst prepared on the initial CeO_2NC oxide only reached a 0.4 wt % loading. In contrast, the one synthesized using the treated oxide, CeO_2NC600, exhibited a final gold loading of 1.0 wt %, i.e. a value 2.5 times larger. The difference is even larger if one considers that the surface area exposed by the treated oxide, 18 $m^2 \cdot g^{-1}$, is roughly half that of the initial CeO_2NC oxide, 38 $m^2 \cdot g^{-1}$. Thus, in terms of gold surface-density, i.e. Au%·m^{-2}, the value corresponding to the 1.0% Au/CeO_2NC600 catalyst, 0.053, is 5-fold that of the 0.4% Au/CeO_2NC one, 0.011.

As commented previously, the hydroxylation and carbonation degrees of the two oxide supports were quite similar, according to FTIR results. Moreover, despite small differences in the carbonation or hydroxylation on the surface of the two CeO_2 samples, to prepare the gold catalysts, the bare oxides were immersed in a Na_2CO_3 solution at pH = 8 during the deposition−precipitation process. This step, very likely, levels off the carbonate and hydroxyl contents on the surfaces of the two support oxides. As seen in Figure S7, the intensities of the carbonate and hydroxyl bands in the DRIFT spectra of the two supported catalysts are also very similar. In the case of the 0.4% Au/CeO_2NC catalyst the fraction of formate species seems larger than in 1.0% Au/CeO_2NC600, as previously observed for the bare oxides.

The quantitative analysis of the C 1s region of the XPS spectra of the two supported catalysts confirms this idea, Figure S8. After deconvolution, the signal corresponding to carbonates, in the energy range 288−292 eV, could be extracted. The values of the C 1s/Ce 3d ratios obtained from the deconvoluted signals indicated the same values for both catalysts, 0.14, which clearly proves the same relative intensity of carbonation in both materials, in good agreement with DRIFT results. Additionally, according to XPS, the surface of the two catalysts was completely free from any trace of chloride species, remnant from the deposition−precipitation of gold.

Therefore, the differences in final gold loadings cannot be related to differences in surface chemistry between the two bare oxides. Likewise, from the FTIR results it is obvious that after gold deposition the chemical state of the surface of the two

DOI: 10.1021/acscatal.5b00086
ACS Catal. 2015, 5, 3504−3513

catalysts, in terms of hydroxylation and carbonation, is also equivalent.

Importantly, these results make clear that the ability of ceria to nucleate and grow gold nanoparticles using the DP method depends quite strongly on the exact crystallographic nature of the facets exposed at the surface by the oxide nanoparticles. In our study, the catalyst with lower surface area exhibits a much higher gold loading. Hence, the quality of the exposed surfaces appears as a much more influencing factor than the total quantity of available surface. To the best of our knowledge, such an important, fundamental question had not been reported yet.

Moreover, the treatments applied to the oxide prior to deposition of gold are key in determining their ability to deposit surface gold nanoparticles. Regarding this point, it seems clear that the surface structure imposed by the {111}-nanofaceting process, induced by oxidation, increases in a large extent the efficiency in gold deposition onto ceria. The influence on DP of a large number of variables (concentration of the gold precursor[32] or of the precipitating agent,[32,33] nature of support and its surface area,[34] precipitation pH,[35] deposition time and temperature[35] or, even, effects of the cleaning and storage steps[32]) has already been established, but the conclusion just stated has not been previously reported. This is possibly due to the difficulties imposed by the use, in previous studies, of high surface area ceria supports. Complex agglomerates of morphologically ill-defined nanocrystals constitute these supports and determining changes in surface crystallography by (S)TEM techniques starting from this situation becomes nearly impossible. Only on the basis of well-defined, morphologically homogeneous, nano-oxide samples as those used here, it is possible to reveal these slight modifications.

According to previous studies,[36] an oxidation treatment at 250 °C guarantees transformation of the gold precursor phase deposited on the surface of ceria based oxides during deposition−precipitation using either urea or sodium carbonate as precipitating agent. TPO-MS experiments show that, at this temperature, evolution rates related to the transformation of the gold precursor into gold reach their maximum. On the other hand, DDP analysis of the HREM images of the supported nanoparticles clearly reveals (Figure 5) the *d*-spacings (d_{111} = 0.233 nm and d_{200} = 0.201 nm) and angles characteristic of fcc metallic gold.

Figure 6 shows HAADF-STEM images representative of the two Au catalysts, Figure 6a and b. Note that the Au nanoparticles can be clearly identified in both catalysts using this imaging technique and also that they exhibit very similar

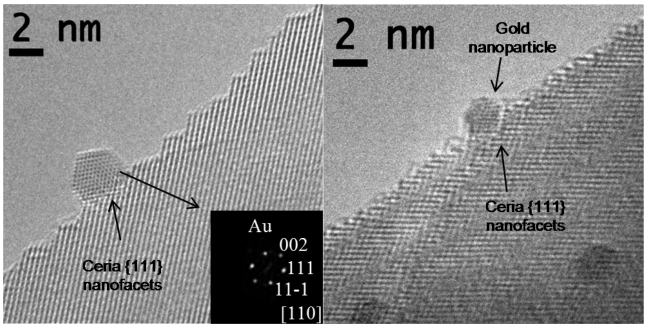

Figure 5. HREM images of the 1.0% Au/CeO_2NC600 sample.

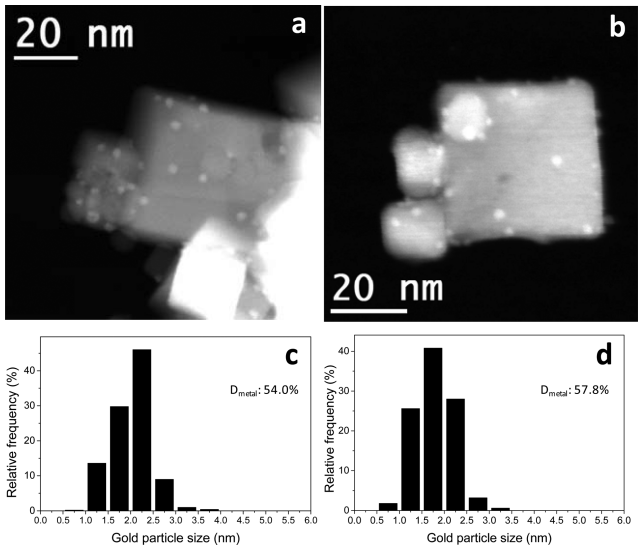

Figure 6. Representative HAADF-STEM images of 0.4% Au/CeO_2NC (a) and 1.0% Au/CeO_2NC600 (b). Corresponding metal particle size distributions are shown in parts c and d, respectively. (inset) Total Au dispersion values (D_{metal}).

sizes. In fact, the gold particle size distributions corresponding to both catalysts established from the whole set of images, Figure 6c and d, are characterized by average particle sizes of 2.0 nm, 0.4% Au/CeO_2NC, and 1.8 nm, 1.0% Au/CeO_2NC600. In spite of depicting a much lower BET surface area, the average Au particle diameter is smaller in the catalyst prepared on the treated oxide. This is also the case for total gold dispersion, whose values are 54% and 58% for the 0.4% Au/CeO_2NC and 1.0% Au/CeO_2NC600 catalysts, respectively. These results indicate that the system of gold nanoparticles in both catalysts is quite similar in terms of dimensions.

Concerning the spatial distribution of the gold nanoparticles on the surface of the ceria support, HAADF images suggest, as previously observed on Au/CeO_2−ZrO_2 and Au/TiO_2 catalysts, that gold nanoparticles deposit preferentially on surface defect sites where the contact area with the support can be increased.[37,38] Thus, in the case of the 1.0% Au/CeO_2NC600 catalyst, particles like those shown in the HREM images of Figure 5 were frequently found. Note that in those valley-like locations the Au particles contact simultaneously at least two {111} facets, this allowing to increase significantly the interface area with the support as compared to a situation where a particle with the same number of atoms sits only on a flat {111} or {100} surface.

To make a first estimate about the distribution of the metal nanoparticles on the surface of the supported catalysts, both individual HAADF-STEM images and those corresponding to the reconstruction of electron tomography experiments were carefully analyzed. High magnification HAADF-STEM images like those shown in Figure S9(a) and (b) clearly indicate that the gold nanoparticles in the 0.4% Au/CeO_2NC catalyst preferentially locate in areas close to corners and edges of the nanocubes, i.e., on {110} and flat {111} facets at the corners. The dominant, larger, {100} facets are not populated by Au particles. This is confirmed by the analysis of tomography experiments, Figures S9(c) and (d), where particles located on edges and corners can be clearly visualized.

Figure S10 depicts the results of tomography experiments of the 1.0% Au/CeO_2NC600 sample. Figures S10(a) and (b)

DOI: 10.1021/acscatal.5b00086
ACS Catal. 2015, 5, 3504−3513

show voxel projections of the reconstructed volume where it is clearly seen that Au nanoparticles, represented in yellow, are mainly located on areas close to the cube edges. Figures S10(c) and (d) display representative slices through the reconstructed tomogram, where the position of the nanoparticles at the edges and corners of the nanocubes is undoubtedly illustrated. These data allow estimating a fraction close to 95% of gold nanoparticles sitting on the {111}-nanofaceted areas in the 1.0% Au/CeO_2NC600 catalyst.

This result agrees well with previous electron tomography observations made on a conventional, low surface area, ceria−zirconia−terbia catalyst which showed a preferential distribution of gold nanoparticles on sites of the catalyst surface allowing contact with two {111} support surfaces.[37]

The electronic state of Au in the two catalysts was determined by XPS, Figure 7. To approach as far as possible

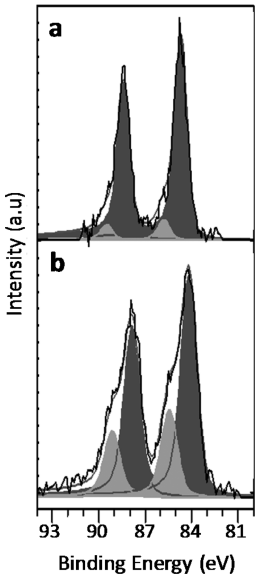

Figure 7. XPS data of the Au/CeO_2 samples. Au 4f core level XPS spectra corresponding to (a) 0.4% Au/CeO_2NC and (b) 1.0% Au/CeO_2NC600 catalysts.

the pretreatment used in the catalytic activity tests, the spectra shown in Figure 7 were recorded after an in situ oxidation treatment at 250 °C followed by evacuation at the same temperature and cooling down in vacuum. A significant difference was found. Thus, for 0.4% Au/CeO_2NC, two different components were identified: one centered at a binding energy of 84.7 eV (dark gray in Figure 7), representing about 91% of the total Au $4f_{7/2}$ contribution, and a small shoulder at 85.8 eV (light gray in Figure 7), corresponding to the remaining 9%. In the Au 4f signal of the 1.0% Au/CeO_2NC600 catalyst, although the two components were also observed, centered at about the same binding energies (84.1 and 85.4 eV, respectively), their relative areas were quite different, the high binding energy contribution increasing up to 28% of the total Au 4f area. These results clearly point out that the oxide pretreatment does not only modify its ability to fix the gold phase but also the overall electronic state of the deposited Au nanoparticles.

According to literature data,[39] the average inelastic mean free path (IMFP) of Au 4f photoelectrons is about 1.78 nm. Taking into account that the XPS signal comes from depths in the samples approximately 3 times the IMPF, the gold signal detected in our experiments would represent the state of roughly the whole set of atoms in the particles since, according to the size distributions in Figure 6, they are all included in particles whose diameter is below 5 nm. This would also explain that the values of the Au 4f/Ce 4d ratios in the two catalysts (0.0108 for 0.4% Au/CeO_2NC and 0.0230 for 1.0% Au/CeO_2NC600) scale well with the total gold loadings.

Concerning the absolute values of binding energies for the two type of Au $4f_{7/2}$ signals described above, we should recall that the position of this peak on a bulk Au^0 sample appears at 84.0 eV whereas it shifts up to 84.4 eV in gold catalysts supported on ceria oxides containing nanoparticles with dispersion in the order of 50%.[40] In the case of the signal attributable to Au^{3+}, it appears at 85.7 eV in bulk Au_2O_3 but at much higher values, 87.6 eV, in supported catalysts in which Au is present as a precursor phase.[31] From these reference values, it seems that the binding energy observed for the most intense peak in 0.4% Au/CeO_2NC is close to the bulk Au^0 values but slightly above (≈0.3 eV) the values of zerovalent gold in small nanoparticles of similar size. In the case of the 1.0% Au/CeO_2NC600 catalyst, the major signal appears at a value nearly 0.3 eV below the Au^0 signal in nanoparticles, whereas the second contribution, which represents roughly one-third of the total gold atoms, appears also shifted 1.0 eV with respect to Au^0 but, oppositely in this case, up in the binding energy scale. This second signal, which was also observed in the 0.4% Au/CeO_2NC catalyst, only represents in that case a minor fraction of 9% of the total gold atoms. These results would suggest a more negative oxidation state in the 0.4% Au/CeO_2NC than in the reference supported gold catalysts and a much larger, 3-fold, contribution of gold atoms in slightly positive oxidation state in 1.0% Au/CeO_2NC600.

Concerning these XPS results, Kim et al.[41] have reported, from DFT calculations performed on a model consisting in Au_{13} clusters supported on CeO_2 that the total Bader charge of the cluster strongly depended on the reduction degree of the ceria support. Thus, for a cluster supported on a fully oxidized support the total charge was +0.22 whereas it changed down to −1.38 after introducing three oxygen vacancies in areas underneath the gold cluster. In both cases the atoms more affected are those at the interface, i.e., in the plane in direct contact with the oxide support. Likewise, in a detailed study of the structure of {100}, {110}, and {111} surfaces of CeO_2 nanocubes by aberration-corrected HREM, Lin et al.[21] found that {111} surfaces present mostly an O termination, whereas the {100} present a mixture of Ce, O and Ce−O terminated patches. On its hand, flat {110} facets contain about 30% oxygen vacancies. Taking all these results into account, it seems at least reasonable that in the initial oxide, dominated by the contribution of {100} facets, the electronic state of gold atoms could be, in general, shifted in the direction of slightly negative species. Also, that the increasing contribution of {111} nanofacets, after the oxidation treatment at 600 °C, could lead to the appearance of a larger fraction of gold atoms exhibiting a slightly positive oxidation state. Somehow, this latter contribution appears as a fingerprint of the system of {111} nanofacets. In this respect we should recall that in the catalyst prepared on the nontreated oxide these {111} nanofacets are not present and that they largely increase in extent after oxidation at 600 °C. Also regarding this point, we should highlight that M. Flytzani-Stephanopoulos et al.[13,42] have reported the appearance of a Au^+ type contribution in the Au 4f XPS signal of a gold catalyst prepared on a CeO_2-NR

DOI: 10.1021/acscatal.5b00086
ACS Catal. 2015, 5, 3504−3513

sample. Although the exact bulk and surface structure of this type of nanostructure is still a matter of debate, some authors have proposed that they are made up by assembling multiply twinned CeO_2 nanoparticles, each one consisting of a number of tetrahedral units exposing {111} nanofacets.[15]

The quantitative analysis of the Ce 3d and 4d signals in the XPS results of the 0.4% Au/CeO_2NC and 1.0% Au/CeO_2NC600 catalysts just as prepared, i.e. after a final oxidation step at 250 °C, indicate the presence of negligible amounts (<1%) of Ce^{3+} in both catalysts. The analysis of cerium XPS signal indicates in this case the presence of 4% and 12% mol. Ce^{3+} species on the surface layers of the 0.4% Au/CeO_2NC and 1.0% Au/CeO_2NC600 catalysts, respectively. This points out that the former is less reducible. This can be properly rationalized by considering that the metal loading of the 1.0% Au/CeO_2NC600 catalyst is much higher, 2.5 times, than that of 0.4% Au/CeO_2NC and that its surface area is smaller. Since the particle size distribution of the two catalysts is roughly the same, the 1.0% Au/CeO_2NC600 catalyst contains a much larger number of particles on its surface per unit surface area. Since removal of oxygen during the evacuation treatment under vacuum at 250 °C most likely involves oxygen back-spillover through the metal nanoparticles,[43,44] it is expected that the reduction degree becomes larger in the catalyst with higher number of particles on its surface.

Concerning this behavior of the Au supported catalysts; we should take into account that the presence of metal nanoparticles on top of ceria nanocrystals strongly modifies the reducibility of the underlying cerium oxide. Thus, in the case of treatments under hydrogen, it is well-established[45−49] that in noble metal loaded catalysts, reduction of ceria takes place at much lower temperatures than in the bare oxides. More important, the presence of supported metal nanoparticles erases the differences in the reduction behavior of bare support oxides whose reduction profiles differ largely.[49] This is attributed to the activation of the H_2 dissociation process by the metal nanoparticles and further spillover of hydrogen-related species onto the support, which are able to produce the oxide reduction at much lower temperatures.[50] This is a major general question that has to be taken into account when comparing the reducibility of ceria based catalysts. In the case of treatments under vacuum, the metal nanoparticles also play a very important role, the reducibility of the supported metal systems being in this case opposite to that of the bare oxides.

Recently, Goris et al.,[51] using electron tomography in EELS mode, have mapped the spatial distribution of Ce^{3+} in cuboctahedral type nanocrystals and found that these species accumulate preferentially beneath {100} facets. This suggests that in the case of the 1.0% Au/CeO_2NC600 catalyst the actual reduction degree under the {111} nanofacets is expected to be smaller than under the remaining {100} extended facets. At this respect it is interesting to analyze the shift of the binding energies of the Au $4f_{7/2}$ signals in the XPS spectra of the two catalysts. According to data in Table 2, when going from the 0.4% Au/CeO_2NC catalyst to 1.0% Au/CeO_2NC600, the signals corresponding to both types of Au atoms move to lower binding energies (as expected for an overall more reduced state of the support), but the shift corresponding to the more positive species ($\Delta BE(Au_2)$ = 0.4 eV) is smaller than that of the less positive one ($\Delta BE(Au_1)$ = 0.6 eV). These results agree well with both a larger reduction degree in the 1.0% Au/CeO_2NC600 catalyst and the differences in the spatial distribution of Ce^{3+} species between the two types of facets.

Table 2. Quantitative XPS Results of the 0.4% Au/CeO_2NC and 1.0% Au/CeO_2NC600 Samples

	0.4% Au/CeO_2NC	1.0% Au/CeO_2NC600
Au 4f/Ce 4d	0.0108	0.0230
BE Au_1 $4f_{7/2}$	84.7	84.1
% Au_1	91	72
BE Au_2 $4f_{7/2}$	85.8	85.4
% Au_2	9	28
% Ce^{3+}	4	12

Finally, the performance of the two catalysts in the CO oxidation reaction was characterized to check the influence of the nanofaceting process on catalytic properties. Figure 8 shows

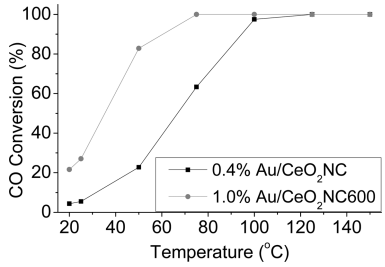

Figure 8. CO oxidation activity values at selected temperatures for 0.4% Au/CeO_2NC and 1.0% Au/CeO_2NC600 samples. Plotted values correspond to steady state measurements at each temperature.

the corresponding CO conversion curves as a function of reaction temperature on the two catalysts. As expected, the 1.0% Au/CeO_2NC600 catalyst is much more active than the 0.4% Au/CeO_2NC. To take into account the differences in the Au loading between the two catalysts and make a meaningful comparison, intrinsic activities (activity per surface gold atom or also called TOFs for turn over frequencies) were estimated, Table 3. For this estimation the activity of the two catalysts

Table 3. CO Oxidation Conversion at 20 °C, Metal Dispersion and TOFs of the Au/CeO_2 Samples Using the Gold Atoms at the Surface (TOF_s) and at the Perimeter (TOF_p) of the Gold Nanoparticles

	0.4% Au/CeO_2NC	1.0% Au/CeO_2NC600
X_{CO} (%)	4.3	20.2
D_{metal} (%)	54.0	57.8
TOF_s (s^{-1})	0.12	0.20
TOF_p (s^{-1})	0.48	0.70

($mol_{converted\ CO} \cdot mol_{Au}^{-1} \cdot s^{-1}$) at 20 °C were used, Figure S11. At this temperature, the total conversion of CO in both catalysts is still very low, and the reaction rate values limited by diffusional processes can be ruled out. Note that the TOF value of the 1.0% Au/CeO_2NC600 catalyst is 67% higher than that of 0.4% Au/CeO_2NC, which is clearly a less active material. These differences cannot be attributed to differences in particle size, since the particle size distributions are quite similar.

There is an increasing consensus about the key role of gold atoms at the perimeter of the gold nanoparticles in the CO oxidation reaction.[41,52−57] Taking this into account, a reasonable interpretation to the higher activity results observed on the 1.0% Au/CeO_2NC600 sample could be linked to the

DOI: 10.1021/acscatal.5b00086
ACS Catal. 2015, 5, 3504−3513

increased value of the perimeter of the supported gold nanoparticles in this catalyst.

To estimate the contribution of this structural factor to the catalytic activity of the gold nanoparticles some structural models were built and analyzed. As shown in Table S1, particles of 1, 2, and 3 nm in diameter were considered to cover the size range of the particle size distributions. The first represents the particles with the smallest diameters; the second corresponds to a particle with the surface averaged diameter and the third one to the particles with the largest size. For each particle size two configurations were considered: (1) on top of a flat surface and (2) located within two {111} nanofacets. After modeling, the number of atoms in the perimeter of the particle was determined.

From Table S1 it seems clear that when the particles locate within the valleys of a {111}-nanofaceted surface, the fraction of Au atoms at the perimeter increases. The increase, which is larger for the bigger particles, ranges roughly from 10 to 20%. Similarly as total dispersion (fraction of metal atoms at the surface of the nanoparticles, $D_{metal} = N_s/N_t$, where N_s is the total number of atoms at the surface and N_t is the total number of metal atoms), a perimeter dispersion (fraction of atoms located at the perimeter of the metal nanoparticles, $D_p = N_p/N_t$ with N_p number of atoms at the perimeter) can also be estimated. Turnover frequencies using D_p, TOF_p, were calculated. The values obtained were 0.48 and 0.70 for 0.4% Au/CeO_2NC and 1.0% Au/CeO_2NC600 respectively (Table 3). It appears that the change in the fraction of gold atoms at the perimeter of the nanoparticles cannot fully account for the 46% improvement in catalytic activity observed for the 1.0% Au/CeO_2NC600 catalyst. Additional factors, such as the oxidation state of the metal atoms (as detected by XPS) or the exact structure of the contacts at the Au||CeO_2 interface must be also contributing to the catalytic activity. In this respect we have to consider that the interface involves in 0.4% Au/CeO_2NC {100}, smooth {110}, and flat {111} planes whereas in the 1.0% Au/CeO_2NC600 catalyst the contact is mostly established with two {111} nanofacets. Our results connect the increase of the slightly positive oxidation states with the development of a much larger Au||{111} perimeter zone, but both effects cannot be properly disentangled from our data.

In any case, our findings reveal that pretreating the oxide before the deposition of gold contributes to largely increase the "apparent" intrinsic activity of the gold atoms on the surface of the catalysts, even when the size distribution of the supported particles is not significantly changed.

CONCLUSION

Summarizing the whole set of results, the use of morphologically defined CeO_2 samples, in the form of nanocubes, has allowed unveiling the influence of oxidation treatments at high temperature (600 °C) on surface nanostructure. In particular, an increase in the extent of truncations at the corners and edges of the cube takes place, which gives rise to an increasing contribution of {111} nanofacets. The appearance of this system of well-developed nanosized {111} facets leads to major changes in the behavior of ceria as support of gold. Thus, in spite of a severe reduction in the specific surface area after the treatment, the oxide increases dramatically its ability to fix gold species on its surface, this contributing to improve the efficiency in the use of the noble metal in DP preparations. The deposited phase depicts total dispersion values similar to those observed in preparations that involve a surface density of gold atoms (number of Au atoms·nm^{-2}) five times smaller, which is also a quite remarkable feature. A change in the electronic state of part of the deposited gold atoms is observed in parallel with the appearance of the {111} nanofacets. Also quite important from the functional point of view, surface nanostructuration leads to an overall 83% increase in the intrinsic activity of the catalyst.

Finally we should highlight that the large influence of oxidizing pretreatments on the preparation and performance of ceria supported gold catalysts could have hardly been determined without the involvement of oxide samples with well controlled morphology and nanosized dimensions.

METHODS

The catalysts prepared for this study were synthesized employing a two-step preparation process. The ceria oxide nanocubes, CeO_2NC (38 $m^2 \cdot g^{-1}$), were obtained by a hydrothermal method previously reported elsewhere.[1] $Ce(NO_3)_3 \cdot 6H_2O$ and NaOH, from Alfa Aesar, were used without further purification (99.5% and 98%, respectively). Appropriate amounts of $Ce(NO_3)_3 \cdot 6H_2O$ (115 mL, 0.1 M) and NaOH solutions (125 mL, 11.5 M) were mixed and stirred in a Teflon 300 mL vessel for 30 min. Then, the Teflon reactor was introduced in a stainless steel autoclave and heated at 180 °C for 24 h in an electric oven. After the hydrothermal synthesis, the mixture was cooled down to room temperature, separating the fresh yellowish precipitates from the aqueous solution by centrifugation. The product was washed with deionized water several times and once with ethanol (Panreac, Ethanol Absolute). Finally, the solids were dried in an oven at 80 °C for 24 h. The CeO_2NC600 support (18 $m^2 \cdot g^{-1}$) was prepared oxidizing the CeO_2NC sample in a 60 mL·min^{-1} flow of 5% O_2/He at 600 °C for 1 h.

Gold-CeO_2 catalysts were prepared via a deposition−precipitation (DP) procedure using $HAuCl_4 \cdot 3H_2O$ (99.99%, Alfa Aesar, 6.4 × 10^{-3} M) as the gold precursor, Na_2CO_3 (0.05M) was used as precipitating agent, and 5−7 g of support were employed in each synthesis. The gold precursor was added to the support suspended in an aqueous solution at pH = 8 and at 60 °C for 1 h, under stirring and in the absence of light. After DP, the suspension was further aged in solution under the same conditions for 1 h. The obtained precipitate was filtered and washed with deionized water several times to remove chlorides, and then dried at 100 °C overnight and pretreated under 5% O_2/He at 250 °C. The preparation procedure was similar to that followed by Daly et al.[58] Both preparations 0.4% Au/CeO_2NC and 1.0% Au%CeO_2NC600 were targeted to a final metal loading 1.5 wt %. The final metal loading, confirmed by ICP analysis was 0.4% and 1.0% for the catalysts prepared on CeO_2NC and CeO_2NC600 respectively.

Catalysts were characterized using high resolution electron microscopy (HREM) and high angle annular dark field−scanning transmission electron microscopy imaging (HAADF-STEM). HREM and HAADF-STEM images were acquired both in a JEOL 2010-F and a monochromated FEI Titan^3 60−300 kV double aberration corrected microscope. An electron probe of 0.5 nm of diameter at a camera length of 8 cm was used during the acquisition of the HAADF images recorded in the JEOL 2010F. High-resolution HAADF-STEM images were recorded in the low base FEI Titan^3 60−300 kV microscope equipped with a probe Cs-corrector, operating at 300 kV. Spot size 9, a condenser aperture of 50 μm, and a 128 mm camera length allowed us to obtain an electron probe with a beam

DOI: 10.1021/acscatal.5b00086
ACS Catal. 2015, 5, 3504−3513

current of 0.04 nA and a convergence angle of 16 mrad. The aberrations of the condenser lenses were corrected up to third-order using the Zemlin tableau to obtain a subangstrom electron probe.

Tomography tilt series were acquired in a JEOL 2010F using HAADF-STEM mode. In these experiments the samples were tilted about a single axis with respect the electron beam using a Fischione 2030 Ultranarrow gap tomographic holder. The images were collected every 5° (for the CeO_2NC) and 2° (for 0.4% Au/CeO_2NC and 1.0% Au/CeO_2NC600 samples). The tilt range varied from −65° to +55° for CeO_2NC, −68° to +68°, and −68° to +54° in the case of 0.4% Au/CeO_2NC and 1.0% Au/CeO_2NC600 samples, respectively. To reconstruct the tomograms, the registered tilt series were aligned using the FEI Inspect 3D and TomoJ (a plug-in of ImageJ)[59] software, employing the simultaneous iterative reconstruction algorithm (SIRT) with 20 iterations. The visualization was achieved using AMIRA 4.0.

XPS data were collected with a Kratos Axis Ultra DLD instrument, equipped with monochromatized Al Kα (1486.6 eV). Self-supported pellets of the catalysts were oxidized at 250 °C under flowing 5% O_2/He (60 mL·min^{-1}) and further evacuated under ultrahigh vacuum at 250 °C. This pretreatment was performed in a catalytic cell coupled to the XPS spectrometer, allowing a clean transfer of the pretreated samples to the analysis chamber. The spectra were collected in the fixed analyzer transmission (FAT) mode, with pass energy of 20 eV. Surface charging effects were compensated with the Kratos coaxial neutralization system, and the binding energy (BE) scale was corrected with respect to the Ce^{4+} u‴ signal at 917.0 eV.[60] Spectra processing was performed with CasaXPS software.

Temperature-programmed reduction with hydrogen (TPR-H_2) analyses were performed on 150 mg of catalyst using a Pfeiffer Vacuum Thermostar GSD301T1 mass spectrometer. The samples were first pretreated under 5% O_2/He atmosphere at 500 °C for 1 h. Then, the samples were cooled down under the same atmosphere down to 150 °C. Finally, the flow was switched to He and the samples were cooled down to room temperature. The TPR-H_2 experiments were conducted with a heating rate of 10 °C·min^{-1} from room temperature to 950 °C, under a constant flow rate of 60 mL·min^{-1} of 5% H_2/Ar. The temperature was kept for 1 h at 950 °C.

Infrared spectroscopy in transmission (FTIR) and diffuse reflectance infrared spectroscopy (DRIFT) modes have been employed to study the surface of the samples. FTIR spectra were collected in a Nicolet Magna 550 FTIR spectrometer equipped with a MCT-A cooled detector (4 cm^{-1} resolution, 25 scans). Self-supported wafers of the samples were made by pressing about 30 mg of powder at 5 ton·cm^{-2}. These wafers were introduced into a Pyrex cell with cooled CaF_2 windows, which was attached to a conventional high vacuum system equipped with a manifold for gas flow operation. Before recording the experiments, samples were pretreated under a flow of 5% O_2/He (60 mL·min^{-1}) at 250 °C (10 °C·min^{-1}) for 1 h. Then, the gas was changed to flowing N_2 at the same temperature for 1 h. Finally, spectra were recorded at room temperature. DRIFTS measurements were carried out in a Harrick cell with ZnSe windows, mounted inside the sample compartment of the FTIR spectrometer Thermo-Electron, Nicolet 8700 with a cryogenic MCT detector (4 cm^{-1} resolution, 25 scans). For DRIFTS experiments, the samples (80−100 mg approximately) were deposited on several stacks of metal meshes inside the cell. The IR beam, approximately 200 μm, goes through the upper layer of the catalyst, at the bed forefront. The cell was connected to the feed gases and a cooling system. The composition of the flowing gas was commuted by switching an electronically actuated flow-through valve (Vici-Valco Instruments), which avoids pressure drops during gas exchanges. IR spectra were recorded after the cleaning pretreatment described above for the FTIR measurements. In DRIFTS experiments helium was used instead of nitrogen as inert flow gas.

Catalytic activity tests for CO oxidation reaction were carried out at atmospheric pressure employing 25 mg of the as-prepared samples (diluted with 100 mg of quartz powder). Previously, the samples were pretreated in a constant flow rate of 60 mL·min^{-1} of 5% O_2/He at 250 °C (10 °C·min^{-1}) for 30 min. Afterward, the flow was changed to He (60 mL·min^{-1}) for 1 h at the same temperature. Finally, the sample was cooled until reaching 40 °C under the same He flow. The reaction mixture was 1% of CO, 0.6% of O_2 and He to balance, in gas flow rate of 100 mL·min^{-1}. First, the sample was heated to 150 °C using a heating rate of 5 °C·min^{-1} and, then, maintained this temperature for 30 min. Afterward, the temperature was decreased in a stepwise manner in 25 °C steps, employing a cooling rate of 2.5 °C·min^{-1}. Finally, the last measurement was recorded at 20 °C. Each temperature interval was maintained for 30 min from 150 °C down to 75 °C and for 75 min at lower temperatures. CO conversion values were measured under isothermal conditions at each step in the cooling process. CO conversion values at each temperature, reported in Figure 8 and Table 3, correspond to those in steady state. The reactants and the products were analyzed by a Bruker CP450 gas chromatograph (GC) equipped with a thermal conductivity detector. Hayesep A (80/100 mesh) and molsieve (13 × 8/100 mesh) columns were attached to the GC to separate and analyze the products.

■ ASSOCIATED CONTENT

Supporting Information

The Supporting Information is available free of charge on the ACS Publications website at DOI: 10.1021/acscatal.5b00086.

Particle size distributions, average particle sizes, surface areas, XRD diagrams, TEM and HAADF-STEM images, electron tomography, TPR-H_2, XPS, FTIR and DRIFT experiments, and theoretical calculations (PDF)

■ AUTHOR INFORMATION

Corresponding Author

*E-mail: jose.calvino@uca.es. Fax: +34-956-016288.

Notes

The authors declare no competing financial interest.

■ ACKNOWLEDGMENTS

The authors acknowledge funding from MINECO/FEDER (MAT2013-40823R and CSD09-00013). Financial resources from the European Union Seventh Framework Programme under Grant Agreement 312483−ESTEEM2 (Integrated Infrastructure Initiative−I3) are also acknowledged. A.B.H. and X.C. thank the Ramón y Cajal Program from the Spanish Ministry of Economy. M.T. acknowledges FPU Grants Program from the Spanish Ministry of Education.

DOI: 10.1021/acscatal.5b00086
ACS Catal. 2015, 5, 3504−3513

REFERENCES

(1) Mai, H. X.; Sun, L. D.; Zhang, Y. W.; Si, R.; Feng, W.; Zhang, H. P.; Liu, H. C.; Yan, C. H. *J. Phys. Chem. B* **2005**, *109*, 24380−24385.
(2) Wu, Z.; Li, M.; Howe, J.; Meyer, H. M.; Overbury, S. H. *Langmuir* **2010**, *26*, 16595−16606.
(3) Wu, Z.; Li, M.; Overbury, S. H. *J. Catal.* **2012**, *285*, 61−73.
(4) Cao, C. Y.; Cui, Z. M.; Chen, C. Q.; Song, W. G.; Cai, W. *J. Phys. Chem. C* **2010**, *114*, 9865−9870.
(5) Cordeiro, M. A. L.; Weng, W.; Stroppa, D. G.; Kiely, C. J.; Leite, E. R. *Chem. Mater.* **2013**, *25*, 2028−2034.
(6) Pan, C.; Zhang, D.; Shi, L.; Fang, J. *Eur. J. Inorg. Chem.* **2008**, *2008*, 2429−2436.
(7) Taniguchi, T.; Katsumata, K. I.; Omata, S.; Okada, K.; Matsushita, N. *Cryst. Growth Des.* **2011**, *11*, 3754−3760.
(8) Yan, L.; Yu, R.; Chen, J.; Xing, X. *Cryst. Growth Des.* **2008**, *8*, 1474−1477.
(9) Yu, T.; Joo, J.; Park, Y. I.; Hyeon, T. *Angew. Chem., Int. Ed.* **2005**, *44*, 7411−7414.
(10) Désaunay, T.; Bonura, G.; Chiodo, V.; Freni, S.; Couzinié, J. P.; Bourgon, J.; Ringuedé, A.; Labat, F.; Adamo, C.; Cassir, M. *J. Catal.* **2013**, *297*, 193−201.
(11) Aneggi, E.; Llorca, J.; Boaro, M.; Trovarelli, A. *J. Catal.* **2005**, *234*, 88−95.
(12) Boucher, M. B.; Goergen, S.; Yi, N.; Flytzani-Stephanopoulos, M. *Phys. Chem. Chem. Phys.* **2011**, *13*, 2517−2527.
(13) Si, R.; Flytzani-Stephanopoulos, M. *Angew. Chem., Int. Ed.* **2008**, *47*, 2884−2887.
(14) Yi, N.; Si, R.; Saltsburg, H.; Flytzani-Stephanopoulos, M. *Energy Environ. Sci.* **2010**, *3*, 831−837.
(15) Florea, I.; Feral-Martin, C.; Majimel, J.; Ihiawakrim, D.; Hirlimann, C.; Ersen, O. *Cryst. Growth Des.* **2013**, *13*, 1110−1121.
(16) Liu, B.; Yao, M.; Li, Z.; Liu, R.; Li, Q.; Li, D.; Zou, B.; Cui, T.; Zou, G.; Liu, J.; Chen, Z. *J. Phys. Chem. C* **2011**, *115*, 4546−4551.
(17) Christou, S. Y.; Efstathiou, A. M. *Top. Catal.* **2013**, *56*, 232−238.
(18) Baudin, M.; Wójcik, M.; Hermansson, K. *Surf. Sci.* **2000**, *468*, 51−61.
(19) Crozier, P. A.; Wang, R.; Sharma, R. *Ultramicroscopy* **2008**, *108*, 1432−1440.
(20) Fronzi, M.; Soon, A.; Delley, B.; Traversa, E.; Stampfl, C. *J. Chem. Phys.* **2009**, *131*, 104701.
(21) Lin, Y.; Wu, Z.; Wen, J.; Poeppelmeier, K. R.; Marks, L. D. *Nano Lett.* **2014**, *14*, 191−196.
(22) Möbus, G.; Saghi, Z.; Sayle, D. C.; Bhatta, U. M.; Stringfellow, A.; Sayle, T. X. T. *Adv. Funct. Mater.* **2011**, *21*, 1971−1976.
(23) Zhang, J.; Gong, X. Q.; Lu, G. *Surf. Sci.* **2015**, *632*, 164−173.
(24) Bhatta, U. M.; Reid, D.; Sakthivel, T.; Sayle, T. X. T.; Sayle, D.; Molinari, M.; Parker, S. C.; Ross, I. M.; Seal, S.; Möbus, G. *J. Phys. Chem. C* **2013**, *117*, 24561−24569.
(25) Aneggi, E.; Wiater, D.; De Leitenburg, C.; Llorca, J.; Trovarelli, A. *ACS Catal.* **2014**, *4*, 172−181.
(26) Binet, C.; Daturi, M.; Lavalley, J. C. *Catal. Today* **1999**, *50*, 207−225.
(27) Busca, G.; Lorenzelli, V. *Mater. Chem.* **1982**, *7*, 89−126.
(28) Collins, S. E.; Baltanás, M. A.; Bonivardi, A. L. *J. Phys. Chem. B* **2006**, *110*, 5498−5507.
(29) Finos, G.; Collins, S.; Blanco, G.; Del Rio, E.; Cíes, J. M.; Bernal, S.; Bonivardi, A. *Catal. Today* **2012**, *180*, 9−18.
(30) Li, C.; Sakata, Y.; Arai, T.; Domen, K.; Maruya, K.; Onishi, T. *J. Chem. Soc., Faraday Trans. 1* **1989**, *85*, 929−943.
(31) Li, C.; Sakata, Y.; Arai, T.; Domen, K.; Maruya, K.; Onishi, T. *J. Chem. Soc., Faraday Trans. 1* **1989**, *85*, 1451−1461.
(32) Dobrosz, I.; Jiratova, K.; Pitchon, V.; Rynkowski, J. M. *J. Mol. Catal. A: Chem.* **2005**, *234*, 187−197.
(33) Zanella, R.; Delannoy, L.; Louis, C. *Appl. Catal., A* **2005**, *291*, 62−72.
(34) Haruta, M. *Catal. Today* **1997**, *36*, 153−166.
(35) Moreau, F.; Bond, G. C.; Taylor, A. O. *J. Catal.* **2005**, *231*, 105−114.
(36) Del Río, E.; López-Haro, M.; Cíes, J. M.; Delgado, J. J.; Calvino, J. J.; Trasobares, S.; Blanco, G.; Cauqui, M. A.; Bernal, S. *Chem. Commun.* **2013**, *49*, 6722−6724.
(37) González, J. C.; Hernández, J. C.; López-Haro, M.; Del Río, E.; Delgado, J. J.; Hungría, A. B.; Trasobares, S.; Bernal, S.; Midgley, P. A.; Calvino, J. J. *Angew. Chem., Int. Ed.* **2009**, *48*, 5313−5315.
(38) Hernández-Garrido, J. C.; Yoshida, K.; Gai, P. L.; Boyes, E. D.; Christensen, C. H.; Midgley, P. A. *Catal. Today* **2011**, *160*, 165−169.
(39) Powell, C. J., Jablonski, A. *NIST Electron Inelastic-Mean-Free-Path Database*; National Institute of Standards and Technology, 2010.
(40) Del Río, E.; Blanco, G.; Collins, S.; Haro, M. L.; Chen, X.; Delgado, J. J.; Calvino, J. J.; Bernal, S. *Top. Catal.* **2011**, *54*, 931−940.
(41) Kim, H. Y.; Lee, H. M.; Henkelman, G. *J. Am. Chem. Soc.* **2012**, *134*, 1560−1570.
(42) Fu, Q.; Saltsburg, H.; Flytzani-Stephanopoulos, M. *Science* **2003**, *301*, 935−938.
(43) Baumgarten, E.; Schuck, A. *Appl. Catal.* **1988**, *37*, 247−257.
(44) Lin, H. *J. Mol. Catal. A: Chem.* **1999**, *144*, 189−197.
(45) Andreeva, D.; Idakiev, V.; Tabakova, T.; Ilieva, L.; Falaras, P.; Bourlinos, A.; Travlos, A. *Catal. Today* **2002**, *72*, 51−57.
(46) Fu, Q.; Weber, A.; Flytzani-Stephanopoulos, M. *Catal. Lett.* **2001**, *77*, 87−95.
(47) Manzoli, M.; Boccuzzi, F.; Chiorino, A.; Vindigni, F.; Deng, W.; Flytzani-Stephanopoulos, M. *J. Catal.* **2007**, *245*, 308−315.
(48) Tabakova, T.; Boccuzzi, F.; Manzoli, M.; Sobczak, J. W.; Idakiev, V.; Andreeva, D. *Appl. Catal., A* **2006**, *298*, 127−143.
(49) Yeste, M. P.; Hernández, J. C.; Bernal, S.; Blanco, G.; Calvino, J. J.; Pérez-Omil, J. A.; Pintado, J. M. *Chem. Mater.* **2006**, *18*, 2750−2757.
(50) Collins, S. E.; Cíes, J. M.; Del Río, E.; López-Haro, M.; Trasobares, S.; Calvino, J. J.; Pintado, J. M.; Bernal, S. *J. Phys. Chem. C* **2007**, *111*, 14371−14379.
(51) Goris, B.; Turner, S.; Bals, S.; Van Tendeloo, G. *ACS Nano* **2014**, *8*, 10878−10884.
(52) Cargnello, M.; Doan-Nguyen, V. V. T.; Gordon, T. R.; Diaz, R. E.; Stach, E. A.; Gorte, R. J.; Fornasiero, P.; Murray, C. B. *Science* **2013**, *341*, 771−773.
(53) Fujitani, T.; Nakamura, I. *Angew. Chem., Int. Ed.* **2011**, *50*, 10144−10147.
(54) Haruta, M. *Faraday Discuss.* **2011**, *152*, 11−32.
(55) Landman, U.; Yoon, B.; Zhang, C.; Heiz, U.; Arenz, M. *Top. Catal.* **2007**, *44*, 145−158.
(56) Rodriguez, J. A.; Ma, S.; Liu, P.; Hrbek, J.; Evans, J.; Pérez, M. *Science* **2007**, *318*, 1757−1760.
(57) Ta, N.; Liu, J.; Chenna, S.; Crozier, P. A.; Li, Y.; Chen, A.; Shen, W. *J. Am. Chem. Soc.* **2012**, *134*, 20585−20588.
(58) Daly, H.; Goguet, A.; Hardacre, C.; Meunier, F. C.; Pilasombat, R.; Thompsett, D. *J. Catal.* **2010**, *273*, 257−265.
(59) Sorzano, C. O.; Messaoudi, C.; Eibauer, M.; Bilbao-Castro, J. R.; Hegerl, R.; Nickell, S.; Marco, S.; Carazo, J. M. *BMC Bioinf.* **2009**, *10*, 124.
(60) Holgado, J. P.; Alvarez, R.; Munuera, G. *Appl. Surf. Sci.* **2000**, *161*, 301−315.

DOI: 10.1021/acscatal.5b00086
ACS Catal. 2015, 5, 3504−3513